

Detection of Gravitational Redshift on the Solar Disk by Using Iodine-Cell Technique *

Y. Takeda¹ and S. Ueno²

© Springer ●●●●

Abstract With an aim to examine whether the predicted solar gravitational redshift can be observationally confirmed under the influence of the convective Doppler shift due to granular motions, we attempted measuring the absolute spectral line-shifts on a large number of points over the solar disk based on an extensive set of 5188–5212 Å region spectra taken through an iodine-cell with the Solar Domeless Telescope at Hida Observatory. The resulting heliocentric line shifts at the meridian line (where no rotational shift exists), which were derived by finding the best-fit parameterized model spectrum with the observed spectrum and corrected for the earth’s motion, turned out to be weakly position-dependent as $\approx +400 \text{ m s}^{-1}$ near the disk center and increasing toward the limb up to $\approx +600 \text{ m s}^{-1}$ (both with a standard deviation of $\sigma \approx 100 \text{ m s}^{-1}$). Interestingly, this trend tends to disappear when the convective shift due to granular motions ($\approx -300 \text{ m s}^{-1}$ at the disk center and increasing toward the limb; simulated based on the two-component model along with the empirical center-to-limb variation) is subtracted, finally resulting in the averaged shift of 698 m s^{-1} ($\sigma = 113 \text{ m s}^{-1}$). Considering the ambiguities involved in the absolute wavelength calibration or in the correction due to convective Doppler shifts (at least several tens m s^{-1} , or more likely up to $\lesssim 100 \text{ m s}^{-1}$), we may regard that this value is well consistent with the expected gravitational redshift of 633 m s^{-1} .

Keywords: Gravitational Redshift; Spectrum, Visible; Velocity Fields, Photosphere

1. Introduction

Ever since Einstein (1911) predicted based on his general theory of relativity that the wavelengths of solar spectrum lines should be shifted redward by a

¹ National Astronomical Observatory of Japan, 2-21-1
Mitaka, Tokyo 181-8588, Japan
email: takeda.yoichi@nao.ac.jp

² Kwasan and Hida Observatories, Kyoto University,
Kurabashira, Kamitakara, Takayama, Gifu 506-1314, Japan
email: ueno@kwasan.kyoto-u.ac.jp

*Based on data collected at Hida Observatory, Kyoto University.
Tables 3 and 4 are presented only as electronic materials.

proportion of 2×10^{-6} ($\approx 600 \text{ m s}^{-1}$ in the velocity scale) as compared to the laboratory wavelengths, a number of solar physicists have tried to confirm this “solar gravitational redshift” observationally. Although very few people nowadays doubt the practical validity of this prediction from general relativity, given the remarkable success in detecting this effect to a high precision from ground-based experiments, such as the well-known Pound–Rebka experiment using the Mössbauer effect (Pound and Rebka, 1960) or the experiment using two hydrogen masers on the ground and on a spacecraft (Vessot *et al.*, 1980), efforts of solar astronomers toward confirming this gravitational redshift in the spectrum of the Sun have been non-terminating and continuing up to now. Apart from the historical studies in the early time of first 50 years which are reviewed in Forbes (1961), several notable trials using modern techniques and/or observational data of higher quality have been done over the last 50 years, as briefly summarized in Table 1.

While the authors of these studies in Table 1 reported that they somehow detected the predicted redshift even to a quantitatively satisfactory degree, their results are not yet necessarily convincing, since they do not seem to have properly taken into consideration the effect of convective shifts due to granular motions and the closely related problem of line-shift determinations (*i.e.*, definition of centroid wavelength) in case of asymmetric line profiles. Besides, most of these investigations are based on observations only on the disk center (or several disk points at best). Given that the well-known center-to-limb variation of the spectral line shift (*i.e.*, the shift increasing redward toward the limb, often called “solar limb effect,” first discovered by Halm (1907)) is regarded to be related with the photospheric velocity fields, it is highly desirable to study absolute line-shifts on a *large* number of disk points while considering the convective shifts (varying from point to point) at the same time. Namely, if the resulting residual shifts obtained from many points are confirmed to be nearly position-independent, it may suggest that shifts due to granular motions are successfully removed.

Recently, we carried out an extensive spectroscopic study of solar differential rotation based on the spectra collected at a large number (≈ 3000) of points over the solar disk while applying the iodine-cell technique for Doppler-shift measurements (Takeda and Ueno, 2011; hereinafter referred to as Paper I). Since these data are suitable for the purpose mentioned above, we decided to conduct absolute Doppler shift measurements by using these spectra, while paying special attention to their subset observed on the solar meridian where the rotational shift is irrelevant, in order to examine how and whether the solar gravitational redshift may be successfully confirmed by eliminating the shifts of velocity-field origin. This is the aim of this investigation.

The remainder of this paper is organized as follows. The observational data are explained in Section 2, and Section 3 describes our adopted method of analysis for absolute line-shift measurements. The resulting solutions and the simulation for the convective shifts to be subtracted are described in Sections 4 and 5, respectively, based on which the final results for the solar gravitational redshift are discussed in Section 6. The conclusion is summarized in Section 7. Finally, a supplementary section is presented as an appendix, where the limb effect empirically studied by Balthasar (1984) is reformulated for our application.

2. Observational Data

We use the same observational data as adopted in Paper I, which were obtained on 20 and 21 July 2010 by using the 60 cm Domeless Solar Telescope (DST) with the horizontal spectrograph of the Hida Observatory of Kyoto University (Nakai and Hattori, 1985) and the iodine cell placed in front of the spectrograph slit. One sequence is made up of 13 scanning observations with a step of $\Delta r = R/12$ from the limb to the disk center at a fixed direction angle (θ), and this sequence was repeated at 48 θ -values (with an increment of $7.^\circ5$), resulting in 13×48 points on the disk as a total. The whole set was similarly conducted on each of the two days but with different slit setting; *i.e.*, E–W direction (20 July) and N–S direction (21 July). Since three spectra (at different positions along the direction of the slit) were extracted from one observation, $3744 (= 13 \times 48 \times 3 \times 2)$ spectra in the 5188–5212 Å region (with reference I₂ molecular lines imprinted) covering the entire solar disk were obtained. See Section 2 of Paper I for more details on the observational data. Prior to the analysis, a tentative wavelength calibration was done by using the representative solar lines, and an appropriate λ (wavelength¹) vs. x (pixel number) relation was assigned to each spectrum frame.

We examined the instrumental profile (P_λ) by fitting the observed lamp+I₂ spectrum (D_λ^{obs}) with the modeled spectrum ($D_\lambda^{\text{sim}} \equiv T_\lambda \otimes P_\lambda$) where T_λ is the transmission function of I₂ vapor and \otimes means convolution. Regarding T_λ , we adopt the spectrum (S/N \approx 1000 with the resolving power of $R \approx$ 400000) recorded for the I₂ cell at Lick Observatory in the 5000–6300 Å region by using the Fourier Transform Spectrometer at the McMath telescope of the National Solar Observatories at Kitt Peak (Marcy and Butler, 1992), which was kindly provided by Dr. G. W. Marcy (see also Takeda *et al.*, 2002).

The instrumental profile was modeled by the sum of nine multiple Gaussian functions as $P(v) \propto \sum_{i=-4}^4 a_i \exp[(v-i)^2]$ where v (in km s⁻¹) is measured from the line center. Assuming $a_0 = 1$, we determined the 8 coefficients (a_{-4} , a_{-3} , a_{-2} , a_{-1} , a_1 , a_2 , a_3 , a_4) by requiring the best fit between the modeled and observed spectra in the 5202–5208 Å region (Figure 1a). For a reference purpose, we also tried fitting with the Gaussian instrumental profile ($\propto \exp[-(v/v_m)^2]$) by finding the best-match solution of the parameter v_m . The shape of the resulting $P(v)$ is depicted in Figure 1b, where we can see that the instrumental profile corresponding to our spectra (somewhat more rounded than the Gaussian) does not show any significant asymmetry that may affect absolute determinations of line shifts. The value of FWHM (\approx 5 km s⁻¹) also suggests that the wavelength resolution is $R \approx$ 60000.

¹Unless otherwise explicitly stated, we mean “air wavelength in the standard condition” by this term.

3. Method of Absolute Line-Shift Determination

3.1. Spectrum Modeling

The iodine-cell technique has been extensively applied for precise Doppler shift determinations so far (*e.g.*, spectroscopic search for exoplanets) since the pioneering study of Marcy and Butler (1992) who showed how to accomplish high precision Doppler analysis based on a stellar spectrum with many superimposed I₂ lines. However, its application has been limited essentially to “relative” measurements (*i.e.*, with respect to a template spectrum whose absolute wavelength scale does not need to be precisely calibrated) so far. Since the determination of “absolute” shift is under question in this study, we have to modify Marcy and Butler’s (1992) procedure (see Section 4 of their paper) appropriately. Namely, theoretically simulated spectrum with firmly established absolute wavelength scale must be used as the stellar template spectrum to be referenced.

Generally, in analogy with the profile modeling conventionally used in stellar physics, the theoretical solar intensity spectrum with imprinted I₂ lines at a disk point of direction cosine $\mu[\equiv \sqrt{1 - (x^2 + y^2)/R^2}]$ may be expressed as follows:

$$I_{\text{th}}(\lambda; \mu) \equiv k \{ [I_{\text{intr}}(\lambda; \mu; \xi, A_1, A_2, A_3, \dots) \otimes M_{\text{mt}}(\lambda; \zeta)] \cdot T_{\text{I}_2}(\lambda) \} \otimes P(\lambda), \quad (1)$$

where k is an arbitrary normalization factor, $I_{\text{intr}}(\lambda; \mu)$ is the intrinsic intensity at μ computed from a solar atmospheric model for given ξ (microturbulence) and A_1, A_2, A_3, \dots (elemental abundances), $M_{\text{mt}}(\lambda; \mu; \zeta)$ is the broadening function corresponding to macroturbulence ζ , $T_{\text{I}_2}(\lambda)$ is the reference I₂ spectrum mentioned in Section 2, $P(\lambda)$ is the instrumental profile (Figure 1b), and “ \otimes ” denotes convolution (while “ \cdot ” is usual multiplication). Note that such a line-broadening formulation based on the dichotomous micro-/macro-turbulence is nothing but a too simple modeling of actual velocity fields. Given that information for an adequate functional form of M_{mt} is lacking, we move $M_{\text{mt}}(\lambda)$ to the outside of the square bracket in Equation (1) and further approximate $M_{\text{mt}}(\lambda; \mu; \zeta) \otimes P(\lambda)$ by a single Gaussian macrobroadening function $G(\lambda; v_M)$, which is parameterized by the macrobroadening parameter v_M (e -folding width) as $G(v) \propto \exp(-v^2/v_M^2)$.

Thus, we adopt the following model for line-spectrum simulation.

$$\begin{aligned} I_{\text{th}}(\mu, \lambda; k, \Delta\lambda_s, \Delta\lambda_{\text{I}_2}, v_M, A_1, A_2, A_3, \dots) \\ \equiv k \{ [I_{\text{intr}}(\lambda + \Delta\lambda_s; \mu; \xi, A_1, A_2, A_3, \dots) \cdot T_{\text{I}_2}(\lambda + \Delta\lambda_{\text{I}_2})] \} \otimes G(\lambda; v_M). \end{aligned} \quad (2)$$

where $\Delta\lambda_s (\equiv \lambda_s^{\text{app}} - \lambda_s^{\text{ref}})$ and $\Delta\lambda_{\text{I}_2} (\equiv \lambda_{\text{I}_2}^{\text{app}} - \lambda_{\text{I}_2}^{\text{ref}})$ are the apparent wavelength shifts of solar lines and I₂ lines relative to the reference wavelength system (*i.e.*, wavelengths given Table 2 for the former or in Table 3 for the latter), respectively.

The parameters characterizing $I_{\text{th}}(k, \Delta\lambda_s, \Delta\lambda_{\text{I}_2}, v_M, A_1, A_2, A_3, \dots)$ are determined by requiring that $\chi^2 (\equiv \int [I_{\text{th}}(\mu, \lambda) - I_{\text{obs}}(\mu, \lambda)]^2 d\lambda)$ is minimized (*cf.* Takeda (1995) for detailed descriptions of the numerical procedure). When the solutions of $\Delta\lambda_s$ and $\Delta\lambda_{\text{I}_2}$ have been established, the absolute line shift is obtained as

$$\Delta\lambda_{\text{abs}} \equiv \Delta\lambda_s - \Delta\lambda_{\text{I}_2}, \quad (3)$$

since $\Delta\lambda_{I_2}$ is the error (due to instrument instability, *etc.*) to be subtracted from $\Delta\lambda_s$.

3.2. Atomic Line Data for Spectrum Synthesis

As mentioned in Section 3.1, spectrum synthesis calculation for simulating the intrinsic specific intensity spectrum (I_{intr}) is important, which needs to be well reproduce the observed solar spectrum by adequately adjusting the elemental abundances and the macrobroadening parameter. Regarding the calculation of $I_{\text{intr}}(\lambda, \mu)$, we use Kurucz's (1993) WIDTH9 program, which was modified by Y. Takeda to enable spectrum synthesis by including many lines, along with Kurucz's (1993) ATLAS9 solar photospheric model (LTE, plane-parallel model). In addition, since the role of microturbulence is comparatively less significant in line broadening, $\xi = 1 \text{ km s}^{-1}$ is assumed as fixed. As to the atomic line data (wavelengths, oscillator strengths, *etc.*) necessary for this simulation, we adopt the data compiled by Kurucz and Bell (1995). Since trial test calculations suggested the necessity of some adjustments, the following modifications were applied to in the $\log gf$ values of four lines. Fe I 5197.929 ($\log gf = -1.64 \rightarrow -1.34$; increased by 0.3 dex), Fe I 5203.691 ($\log gf = -3.093 \rightarrow -9.99$; neglected), Ni I 5203.788 ($\log gf = -1.163 \rightarrow -9.99$; neglected), and Fe I 5209.884 ($\log gf = -3.26 \rightarrow -3.46$; decreased by 0.2 dex). Besides, since the weak depression at $\lambda \approx 5202\text{\AA}$ could not be reproduced (*i.e.*, relevant line is missing in Kurucz and Bell's database), we neglected (masked) this local feature in χ^2 evaluation.

The finally adopted data for the important lines of appreciable strengths are summarized in Table 2, and how the observed disk-center spectrum (taken from the FTS solar spectrum atlas; Neckel 1994, 1999)² can be fitted with the theoretical calculated $\mu = 1$ intensity spectrum by using these atomic data (with appropriately adjusted elemental abundances and the broadening parameter) is displayed in Figure 2, where the lines given in Table 2 are also identified.

3.3. Strengths and Formation Depths of Spectral Lines

It is necessary to have knowledge on the strength and related quantities (*e.g.*, line-forming depth) of spectral lines existing in the relevant wavelength range (5188–5212 Å), since the convective line shift (its correction is important as will be discussed in Section 5) appreciably depends on such individual line properties. For this purpose, by using the solutions of the elemental abundances derived as by-products of the synthetic spectrum fitting in Section 3.2 (Figure 2), we *inversely* computed EW (equivalent width at the disk center) for all lines presented in Table 2, while assuming that each line is single and isolated (*i.e.*, irrespective of whether they are actually blended or not). Besides, we computed two kinds of line-formation depth; one is the mean formation depth averaged over the profile ($\langle \log \tau \rangle$) and the other is the formation depth at the line-center

²This spectrum atlas is available at <ftp.hs.uni-hamburg.de/pub/outgoing/FTS-atlas> .

$(\log \tau_0)$, which are defined as follows.

$$\langle \log \tau \rangle \equiv \frac{\int R_\lambda \log \tau_{5000}(\tau_\lambda = 1) d\lambda}{\int R_\lambda d\lambda}, \quad (4)$$

where $R_\lambda (\equiv 1 - I_\lambda/I_{\text{cont}})$ is the line depth of the emergent intensity profile, $\tau_{5000}(\tau_\lambda = 1)$ is the continuum optical depth at 5000 Å corresponding to $\tau_\lambda = 1$ at wavelength λ within the profile, and the integration range is over the whole profile.

$$\log \tau_0 \equiv \log \tau_{5000}(\tau_{\lambda_0} = 1) \quad (5)$$

where τ_{λ_0} is the optical depth at the line center. (All these quantities are computed for the $\mu = 1$ ray at the disk center.) The resulting values of EW, $\langle \log \tau \rangle$, and $\log \tau_0$ are given in Table 2.

3.4. Wavelength Scale of I₂ Reference Spectrum

Regarding the reference spectrum of I₂ molecular lines (T_λ), we adopt Marcy and Butler (1992)’s very high-resolution transmittance spectrum of Lick I₂ cell already mentioned Section 2. This standard I₂ spectrum in the relevant wavelength region, which we also used to fit the spectrum of our I₂ cell (Figure 1a), is given in Table 3 (electronic data). Though the original data are represented in terms of the vacuum wavelength scale (λ_{vac}), we converted it into air wavelength (λ_{air} ; which is usually used in optical spectroscopy such as in Kurucz and Bell’s atomic-line database we adopted) as

$$\lambda_{\text{air}} = \lambda_{\text{vac}}/n_{\text{air}}. \quad (6)$$

Here, n_{air} is the refractive index of air in the standard condition represented as a function of the wavenumber $k \text{ cm}^{-1}$ [$= 10^8/\lambda_{\text{vac}}(\text{Å})$], for which we adopted the formula given in Cox (2000):

$$n_{\text{air}} = 1. + 6432.8 \times 10^{-8} + 2949810. / (146. \times 10^8 - k^2) + 25540. / (41. \times 10^8 - k^2). \quad (7)$$

While this Lick I₂ spectrum has so far been successfully used for very precisely detecting “relative” variations of radial velocity intended for exoplanet search or stellar seismology, it is not clear whether its “absolute” wavelength scale is sufficiently reliable. Since this point is of primary importance in this study, we examined its precision by comparing it with the theoretical I₂ spectrum by using “IodineSpec” program (Knöckel *et al.*, 2004), which can model the wavelengths of the rovibronic structure of the I₂ B–X spectrum with very high precision (its uncertainty is on the order of only $\approx 30 \text{ MHz}$ at $\approx 5200 \text{ Å}$, which means a precision of $\approx 5 \times 10^{-8}$ or $\approx 15 \text{ m s}^{-1}$; *cf.* their Figure 3), though the intensity distribution is not so precisely reproduced as wavelengths. The comparisons are displayed in Figures 3a (wide view) and 3b (magnified view of the 5196–5197 Å region), where the vacuum wavelength scale (λ_{vac}) is used in the abscissa. We notice from Figure 3b that the Lick I₂ spectrum appears to be slightly shifted redwards relative to the theoretical one. This is quantitatively confirmed by

a cross-correlation analysis (Figure 3c), showing that the average shift in this 5196–5197 Å bin amounts to 0.0028 Å or $\approx 160 \text{ m s}^{-1}$. We similarly examined all twenty-four 1 Å-bins in the 5188–5212 Å region and the histogram of the resulting shifts are depicted in Figure 3d, from which we conclude that the absolute wavelength scale of the Lick I₂ spectrum is systematically redder and should be corrected blueward by -167 m s^{-1} (simple average of 24 values; with a standard deviation of 42 m s^{-1}).

Besides, given that we transformed the vacuum wavelengths of reference I₂ spectrum into the air wavelengths by applying Equations (6) and (7), the air wavelengths of the atomic lines we adopted for simulating the solar spectrum have to be essentially on the same system. For the purpose of checking the consistency, we examined the $\lambda_{\text{vac}}/\lambda_{\text{air}}$ ratios (or the refractive index in the air; n_{KB}) for all 719 lines (5188–5212 Å region) included in Kurucz and Bell (1995) as

$$n_{\text{KB}} \equiv (E_{\text{upper}} - E_{\text{lower}})/(10^8 \lambda_{\text{air}}), \quad (8)$$

where E_{upper} and E_{lower} are the excitation potentials of lower and upper levels in cm^{-1} , respectively, and λ_{air} is the air wavelength in Å (all these three kinds of data are presented in Kurucz and Bell’s database). The comparisons of such evaluated n_{KB} ’s and the corresponding formula values (n_{formula}) resulting from Equation (7) are depicted in Figure 4. We can recognize from this figure that the consistency is satisfactorily good and the average of the relative difference $[(n_{\text{KB}} - n_{\text{formula}})/n]$ is only -4.47×10^{-8} (with a standard deviation of $\sigma = 6.46 \times 10^{-8}$) or -13 m s^{-1} ($\sigma = 19 \text{ m s}^{-1}$).³ Thus, even though small, we formally apply a correction of $-(-13) \text{ m s}^{-1}$ to the air wavelengths of I₂ lines (*cf.* given 3rd column of Table 3) in order to maintain consistency with the wavelengths of atomic lines given in Table 2. (Regarding the sign of the correction, since $\lambda_{\text{air}}^{\text{formula}} < \lambda_{\text{air}}^{\text{KB}}$ because of $n_{\text{KB}} < n_{\text{formula}}$, we have to shift $\lambda_{\text{air}}^{\text{formula}}$ slightly redward to make it consistent with Kurucz and Bell’s system.)

Consequently, we conclude that the $\lambda_{\text{I}_2}^{\text{ref}}$ values given in Table 2, which we adopt as the reference (air) wavelengths of I₂ lines, should be corrected blueward by $\delta\lambda_{\text{I}_2}^{\text{ref}} = -154 \text{ m s}^{-1}$ (net combination of -167 m s^{-1} and $+13 \text{ m s}^{-1}$). More precisely, since the wavelengths of I₂ lines directly affect $\lambda_{\text{I}_2}^{\text{ref}}$ of $\Delta\lambda_{\text{I}_2}$ ($\equiv \lambda_{\text{I}_2}^{\text{scale}} - \lambda_{\text{I}_2}^{\text{ref}}$), it is included in $\Delta\lambda_{\text{abs}}$ as the term of positive sign ($+\lambda_{\text{I}_2}^{\text{ref}}$; *cf.* Equation (3)), which means that $\Delta\lambda_{\text{abs}}$ should be corrected by $+\delta\lambda_{\text{I}_2}^{\text{ref}} = -154 \text{ m s}^{-1}$. In practice, the whole fitting analysis is conducted by literally using the (air) wavelengths of I₂ spectrum given Tables 3, and this correction is applied to the results at the last stage.

³This dispersion (σ) of $\approx \pm 20 \text{ m s}^{-1}$ is reasonably attributed to the fact that the wavelengths of Kurucz and Bell’s (1995) line data are presented only to the third decimal of Å (*cf.* Table 2), which means that the intrinsic uncertainty amounting up to $\lesssim 0.0005 \text{ Å}$ or $\lesssim 30 \text{ m s}^{-1}$ is inevitable in our analysis.

4. Results

Although our primary interest is only on the meridian points ($x \approx 0$) unaffected by the rotational velocity, we carried out our absolute wavelength-shift analysis for all the available data points over the entire solar disk, except for those at the limb because the solutions there were found to be comparatively uncertain and unstable (*i.e.*, the data at r_{12} were not used; *cf.* Figure 2 in Paper I).

Our spectrum covering 5188–5212 Å was divided into four segments of 5–6 Å [regions (a), (b), (c), and (d), *cf.* Table 2], and $\Delta\lambda_{\text{abs}}^i$ was determined for each segment i ($i = 1, 2, 3, 4$; each corresponding to a, b, c, d, respectively) by applying the procedure described in Section 3.1. An example of how the observed solar+I₂ spectrum matches the modeled spectrum corresponding to the best-fit solutions of the parameters is demonstrated in Figure 5. Then, the (raw) radial velocity of the observed point on the solar surface ($V_{\text{r}}^{\text{raw}}$) and its probable error (ϵ) were computed as

$$v_i \equiv c\Delta\lambda_{\text{abs}}^i/\lambda_i - 154 \text{ (m s}^{-1}\text{)}, \quad (9)$$

$$V_{\text{r}}^{\text{raw}} \equiv \frac{\sum_{i=1}^N v_i}{N}, \quad (10)$$

and

$$\epsilon \equiv \sqrt{\frac{\sum_{i=1}^N (v_i - V_{\text{r}}^{\text{raw}})^2}{N(N-1)}}, \quad (11)$$

where we applied the correction of -154 m s^{-1} due to the absolute wavelength scale problem of the adopted I₂ spectrum (Section 3.3), c is the speed of light, and $N = 4$. Further, we added the heliocentric correction for the earth’s motion (Δ^{hel} ; *cf.* Section 4.1 in Paper I) and obtained $V_{\text{r}}^{\text{hel}}$ in the heliocentric system as

$$V_{\text{r}}^{\text{hel}} = V_{\text{r}}^{\text{raw}} + \Delta^{\text{hel}}. \quad (12)$$

Figure 6 demonstrates, for the meridian case, how the results of V_{r} obtained at different observational times become mutually consistent by applying the Δ^{hel} correction.

The distribution of the probable error (ϵ) for each measurement is shown in Figure 7, which is directly comparable with Figure 9 of Paper I. As can be seen from Figure 7a, ϵ mostly ranges between $\approx 50 \text{ m s}^{-1}$ and $\approx 100 \text{ m s}^{-1}$; that is, by ≈ 2 –3 times larger than the case of relative measurements in Paper I, reflecting the difficulty of absolute measurements. We do not see any clear dependence of ϵ upon the position (r) on the disk, except for a slight decrease near to the limb (Figure 7b). The results of our analysis [observational time, (r, θ) as well as (x, y) coordinates, $V_{\text{r}}^{\text{raw}}$, Δ^{hel} , and $V_{\text{r}}^{\text{hel}}$] are presented in Table 4 (electronic data) for the meridian case of our concern, which will be discussed in Section 6.

5. Simulation of Convective Blue-Shift

5.1. Line Shift due to Convective Granular Motions

Although we have derived the absolute line-shift (V_r^{hel}) reduced to the rest system of the Sun at each point on the disk, it alone is still insufficient for our main purpose of quantitatively confirming the gravitational redshift, since the systematic shift due to convective velocity fields has still to be subtracted.

A hot up-rising bright bubble (granular cell) originating from the deeper convective zone gradually decelerates its speed as it moves upward while dissipating its energy, and eventually stops and turns into cool downflows (dark intergranular lane). Since the contribution of the brighter former is larger than the darker latter in the integrated spectrum, the net effect generally makes a blue shift as seen from the observer. Since the extent of velocity contrast is depth-dependent (*i.e.*, becoming less significant toward higher layers), such a blue shift tends to be more appreciable for weak deep-forming lines than strong high-forming lines, as seen in Figure 2 of Allende Prieto and García López (1998). For the same reason, the off-center region (forming deeper) of a line profile is more blue-shifted than the region of line-center core (forming higher), which results in an asymmetric profile with a “C”-shaped bisector (see, *e.g.*, Dravins, 1982).

To make things further more complicated, not only the vertical velocity field but also the horizontal field has to be considered when studying the variation of the convective shifts over the disk. This results in a flatter decreasing rate of blue shift (from disk center toward the limb) compared to the case of the vertical field only; actually, even a peak of blue shift is occasionally observed not the disk center but at off-center around $\mu \approx 0.8$ (Schröter, 1959; Beckers and Nelson, 1978; Balthasar, 1984, 1985).

Considering this complexity, we decided to adopt the following strategy: As far as the convective shift at the disk center ($\mu = 1$) is concerned, we can evaluate it for any relevant line to a sufficient precision, thanks to the availability of a well-tuned two-component model. Meanwhile, since this kind of line shift at positions off the center ($0 < \mu < 1$) is too difficult to simulate, we invoke the empirical work of Balthasar (1984), who extensively investigated the relative μ -dependence of the shifts for many spectral lines of different properties and classified them in terms of line-formation depth, which we reformulated in a more easy-to-use manner (*cf.* the Appendix). Accordingly, as successively described in the following sections, we (1) first simulate the absolute line-shifts at the disk center ($\mu = 1$) for representative lines (Section 5.2), and (2) then combine them with the relative center-to-limb trends empirically elucidated by Balthasar (1984) (Section 5.3).

5.2. Absolute Shift at the Disk Center

For the purpose of simulating the disk-center intensity profile under convective velocity fields, we adopt the two-component model proposed by Borrero and Bellot Rubio (2002). Their model consists of two kinds of plane-parallel atmospheric models (with only vertical velocity fields) corresponding to hot/bright

granular (g) and cool/dark intergranular (i) region. The details are presented in Appendix A in their paper, where T (temperature), P_e (electron pressure), P_g (gas pressure), ρ (density), and v (vertical velocity) are given as functions of depth (along with the depth-independent microturbulence and macroturbulence) for each of the two models. The structures of $T(\tau_{5000})$ and $v(\tau_{5000})$ for each model are depicted in Figure 8a.

By using the WIDTH9 program (as in Section 3) along with these models, we computed the emergent specific intensity profile $I^g(\lambda)$ and $I^i(\lambda)$ at the disk center, from which the final spectrum is eventually obtained as the combination of these two:

$$I^{\text{comb}}(\lambda) \equiv (1 - \alpha)I^g(\lambda) + \alpha I^i(\lambda), \quad (13)$$

where α is the filling factor assumed to be 0.24 according to Figure 3 of Borrero and Bellot Rubio (2002).

In order to check our computational procedure, we simulated the $\mu = 1$ profiles of 22 Fe I lines given in Table 1 of Borrero and Bellot Rubio (2002), and confirmed that most⁴ of the resulting line-shifts satisfactorily reproduced those of the observed line profiles of Neckel's (1994, 1999) solar disk-center spectrum atlas. Figure 8b shows an example of such simulated I^g , I^i , and I^{comb} (each being normalized with respect to the continuum level of its own) for the representative Fe I 5194.941 line.

Such computed $I^{\text{comb}}(\lambda)$ is further convolved with the instrumental profile (P ; *cf.* Section 2), resulting in an asymmetric broadened profile corresponding to our instrumental condition. Profile examples before and after I.P. convolution are displayed in Figure 8c again for the case of Fe I 5194.942.

The final step is to determine the line shift from such simulated (asymmetric) profile by applying the same procedure described in Section 3; *i.e.*, fitting with the classically modeled symmetric profile while adjusting the line shift ($\delta\lambda$ or δV) along with the broadening width and the elemental abundance. This process is demonstrated in Figure 8d, where we can see that the match is satisfactory.

We applied the whole above-mentioned procedure to 18 lines of appreciable strengths, which we selected by the criterion of $\langle \log \tau \rangle < -1$. Such determined line shifts (δV_1) at the disk center ($\mu = 1$) for these lines are given in the last column of Table 2, where we can see that δV_1 is in the range of $-310 \text{ m s}^{-1} \lesssim \delta V_1 \lesssim -230 \text{ m s}^{-1}$.⁵

⁴ More precisely, the predicted shifts of the 3 lines (Fe I 6574.2285, Fe I 6581.2100, and Fe I 6739.5220) out of 22 lines appear to be only slightly shifted bluewards compared to the observation; otherwise, the profile/wavelength match for the remaining lines was found to be very good.

⁵ It should be stressed that we adopted the fitting-based line-shift (δV_{fit}), while the line shift (δV_{min}) defined in terms of the wavelength of minimum intensity has been more commonly used so far. We also determined δV_{min} by interpolating the lowest three profile points by a quadratic function (see, *e.g.*, Allende Prieto and García López, 1998) for all these 18 lines in the present case, and found that the difference $\delta V_{\text{min}} - \delta V_{\text{fit}}$ tends to be EW-dependent, which varies from -60 m s^{-1} (EW $\approx 70 \text{ m}\text{\AA}$) to $+120 \text{ m s}^{-1}$ (EW $\approx 230 \text{ m}\text{\AA}$) and can be approximated by the linear-regression relation $\delta V_{\text{min}} - \delta V_{\text{fit}} (\text{m s}^{-1}) = -129 + 1.02\text{EW} (\text{m}\text{\AA})$. Since the typical extent of this difference is several tens of m s^{-1} , we may state that the results are not seriously influenced by the definition of line shift.

5.3. Center-to-Limb Variation of δV

We are now ready to derive the μ -dependent convective shift, δV_μ , by combining the disk-center δV_1 computed in Section 5.1 and the center-to-limb variation formulated in the Appendix based on the results of Balthasar (1984).

For a line k , we first evaluate $\log \tau_B^k$ (Balthasar's core-forming depth) from $\log \tau_0^k$ (our line-center-forming depth) by solving Equation (23). Then, the coefficients b^k and c^k in the velocity unit can be derived from Equations (21), which are sufficient with Equation (19) to establish the relative μ -dependence of δV as

$$\delta V^k(\mu) - \delta V^k(1) = \Delta v_B^k(\mu) - \Delta v_B^k(1) = b^k(1 - \mu) + c^k(1 - \mu)^2. \quad (14)$$

Therefore, combining Equation (14) with δV_1^k which was already derived in Section 5.2, we can express the absolute convective shift for line k at any μ as

$$\delta V_\mu^k = \delta V_1^k + b^k(1 - \mu) + c^k(1 - \mu)^2. \quad (15)$$

Such obtained position/angle-dependent δV_μ^k results for the 18 lines are shown in Figure 11a (δV vs. μ) and 11b (δV vs. $\sqrt{1 - \mu^2}$), where we can see that the tendencies are nearly similar to each other, except for two conspicuously strong Cr I lines (at 5206.038 and 5208.419 Å) of low excitation ($\chi_{\text{low}} \approx 1$ eV).

As the final step, we average these δV_μ results over 18 lines in order to obtain the mean relation, while adopting

$$w^k \propto 1/\langle \tau^k \rangle \equiv 10^{-(\log \tau^k)} \quad (16)$$

as the weight⁶ for line k .

Accordingly, we finally obtain

$$\begin{aligned} \langle \delta V_\mu \rangle &= \langle \delta V_1 \rangle + \langle b \rangle(1 - \mu) + \langle c \rangle(1 - \mu)^2 \\ &= -278.5 + 79.9(1 - \mu) + 422.3(1 - \mu)^2 \quad (\text{m s}^{-1}), \end{aligned} \quad (17)$$

where $\langle \dots \rangle$ is the w^k -weighted average over 18 lines. Such obtained $\langle \delta V_\mu \rangle$, which is also depicted in Figures 11a and 11b by the thick red line, will be used in Section 6 for correcting V_r^{hel} for the convective shift.

⁶ This choice of weight ($\propto 1/\langle \tau \rangle$) is for the following reason. The precision of radial velocity determination is higher not only for stronger (deeper) but also for sharper (narrower) lines, which means that the radial velocity is mainly determined by sharp saturated lines at the flat part of the curve of growth. Meanwhile, “very” strong lines with appreciable damping wings do not necessarily contribute so significantly because of their less sharpness. We point out here that the extent of saturation (*i.e.*, both of strength and sharpness), to which more weight should be given, is most well described by $1/\langle \tau \rangle$ because it increases as a line gets stronger from the linear to the flat part of the curve of growth, while it then turns to decrease as a line further becomes very stronger and comes into the damping part of the curve of growth, which is the characteristic just what we want. (In contrast, $1/\tau_0$ is ever increasing monotonically with the growth of line strength.) Figure 11d describes well this situation.

6. Discussion

We now discuss the results of absolute line shifts obtained in Section 4, while taking into account the convective-shift correction estimated in Section 5. In the following description, x and y denote the Cartesian coordinates on the solar disk (*cf.* Figure 2a in Paper I). The relations between V_r^{hel} obtained for all the observed points and each of the positional coordinates are displayed in Figures 10a (V_r^{hel} vs. y) and 10c (V_r^{hel} vs. x), where the exhibited trends can be reasonably understood by the Doppler shift due to solar rotation ($V_r^{\text{hel}} \propto x$; *cf.* Section 4.1 in Paper I). A rough inspection of these two figures suffices to realize that V_r^{hel} distributes around $\approx +500 \text{ m s}^{-1}$ at $x \approx 0$ (meridian line) or near to the disk center (where the data points are densely confined), which suggests that V_r^{hel} approaches the expected gravitational shift⁷ of $+633 \text{ m s}^{-1}$ where the rotational Doppler shift is negligible.

In order to study this situation more in detail, we pay attention to the selected dataset corresponding to the observations on the meridian line ($x \approx 0$), which are given in Table 4. The V_r^{hel} vs. y correlation for this subset is shown in Figure 10b, where we can confirm that V_r^{hel} values confine around $\approx +500 \text{ m s}^{-1}$ (with a standard deviation of $\sigma \approx 100 \text{ m s}^{-1}$) as mentioned above. In addition, we can recognize a tendency of slight increase of V_r^{hel} with $|y|$; *i.e.*, $\approx +400 \text{ m s}^{-1}$ at the disk center and increasing toward the limb up to $\approx +600 \text{ m s}^{-1}$. (Actually, such a change of V_r^{hel} from the limb to the center on the meridian line is already observed in Figure 6.) This trend is nothing but the ‘‘limb effect’’ already mentioned in (see, *e.g.*, Figure 2 of Dravins, 1982). Interestingly, when we overplot the $\langle \delta V \rangle$ vs. y relation according to Equation (17) [describing $\langle \delta V \rangle$ as a function of $\mu (= \sqrt{1 - (y/R)^2})$ derived in Section 5, its tendency is found to be similar to the behavior of V_r^{hel} (*cf.* the solid line in Figure 10b). Thus, V_r^{hel} is corrected for $\langle \delta V \rangle$ as

$$V_r^{\text{hel,corr}} \equiv V_r^{\text{hel}} - \langle \delta V \rangle, \quad (18)$$

and the resulting $V_r^{\text{hel,corr}}$ is plotted against y in Figure 10d. We can see in this figure that the slight curvature observed in Figure 10b is more or less removed by this correction (especially in the northern hemisphere, though somewhat over-corrected in the southern hemisphere) and $V_r^{\text{hel,corr}}$ is now nearly y -independent along the meridian line, which is just what we intended to achieve (*i.e.*, to consistently detect the gravitational redshift at a number of different points by eliminating the position-dependent limb effect; *cf.* Section 1). The distribution histogram of $V_r^{\text{hel,corr}}$ and the $\langle V_r^{\text{hel,corr}} \rangle$ (locally averaged value) vs. y relation are shown in Figures 10e and 10f, respectively.⁸ The average of all the $V_r^{\text{hel,corr}}$ (meridian) data turned out to be $\langle \langle V_r^{\text{hel,corr}} \rangle \rangle = 698 \text{ m s}^{-1}$ (with a standard deviation of $\sigma = 113 \text{ m s}^{-1}$).

⁷This value of 633 m s^{-1} corresponds to an observer on the earth while the redshift is 636 m s^{-1} for the observer at infinity.

⁸It is interesting to note that our $\langle V_r^{\text{hel,corr}} \rangle$ of 696 m s^{-1} at the disk center (*cf.* Figure 10f) is comparable to 684 m s^{-1} derived by Balthasar (1985) as the asymptotic value for the absolute disk-center line-shift at the strong-line limit of $\log \tau_B \rightarrow -\infty$ (where the convective shift is expected to be insignificant).

Here, it may worthwhile to recall that several sources of errors are involved in our results: Each individual absolute V_r measurement is accompanied by a probable error of $\approx 50\text{--}100\text{ m s}^{-1}$ (Figure 7). Also, the randomness of granular velocity fields (represented by “wiggly-line” character seen in high-resolution slit-spectrograms) produces an appreciable dispersion of V_r (even though it must have been somewhat smoothed because spatial information over $42''$ has been averaged in our spectrum; *cf.* Section 2 in Paper I), which is estimated in the present case to be on the order of $\approx 100\text{ m s}^{-1}$ (Figures 10e and 10f). Yet, since these are random errors, they could (in principle) be reduced in the averaged $\langle\langle V_r \rangle\rangle$ by summing up as many data as possible; *e.g.*, averaging of all 144 data on the meridian would result in a reduction by a factor of ≈ 10 ($\approx \sqrt{144}$). We thus estimate that the error component in $\langle\langle V_r \rangle\rangle$ due to such random sources would have been reduced to the $\approx 10\text{--}20\text{ m s}^{-1}$ level. Actually, however, systematic errors must be more important, which are hard to evaluate. For example, while we corrected the absolute wavelength-scale of Lick I_2 spectrum by 162 m s^{-1} , this value itself already has an uncertainty with a magnitude of several tens m s^{-1} (Figure 3d). Besides, although our convective-shift corrections turned out seemingly successful, we have no idea about how much systematic errors are involved in these, given that this correction differs from line to line with variations of $\approx 50\text{--}100\text{ m s}^{-1}$ (*cf.* Figure 9). Considering all what described above, we would modestly state that our final $\langle\langle V_r^{\text{hel,corr}} \rangle\rangle$ value suffers inevitable ambiguities of no less than several tens m s^{-1} or maybe amounting up to $\lesssim 100\text{ m s}^{-1}$.

Accordingly, while the resulting $\langle\langle V_r^{\text{hel,corr}} \rangle\rangle$ of 698 m s^{-1} is slightly larger than the predicted gravitational redshift of 633 m s^{-1} by $+65\text{ m s}^{-1}$, this difference is not meaningful in view of the expected uncertainties of several tens m s^{-1} to $\lesssim 100\text{ m s}^{-1}$ as estimated above. We thus conclude that the solar gravitational redshift has been quantitatively confirmed in a reasonable manner by our absolute line-shift analysis using the iodine-cell technique, in combination with the simulated convective shift corrections.

7. Conclusion

Motivated by the situation that various past studies of solar gravitational redshift are not convincing because few of them seem to have properly considered the Doppler shifts due to inhomogeneous convective motions, we decided to examine whether the predicted solar gravitational redshift can be observationally confirmed by removing the appropriately simulated convective shift.

For this purpose, we attempted measuring the absolute spectral line-shifts on a large number of points over the solar disk based on an extensive set of $5188\text{--}5212\text{ \AA}$ region spectra taken through an iodine-cell with the Solar Domeless Telescope at Hida Observatory, where we paid attention only to the selected dataset observed on the solar meridian where the rotational Doppler shift is irrelevant.

In analogy with the analysis technique for precise “relative” shift measurements (from I_2 +object spectra) elaborated by Marcy and Butler (1992), we

developed a method for measuring “absolute” shifts by using the theoretical solar intensity spectrum template, which is computed from a model atmosphere and parameterized by elemental abundances along with the broadening parameter; and the absolute shift can be established by finding the best-fit solution of the parameterized model spectrum with the observed spectrum.

The resulting heliocentric absolute shifts (V_r^{hel}) on the meridian line turned out to be weakly position-dependent as $\approx +400 \text{ m s}^{-1}$ near the disk center and increasing toward the limb up to $\approx +600 \text{ m s}^{-1}$ (both with a standard deviation of $\approx 100 \text{ m s}^{-1}$).

We then simulated the convective blue shifts for representative 18 lines by using Borrero and Bellot Rubio’s (2002) two-component model for the disk center, combined them with the empirical relations of relative center-to-limb variation investigated by Balthasar (1984), and finally adopted the weighted-average over 18 lines. The resulting shift is $\langle \delta V \rangle \approx -300 \text{ m s}^{-1}$ at the disk center, gradually increases to $\approx -100 \text{ m s}^{-1}$ at $|y/R| \approx 0.9$, and shows a suddenly increase up to $\approx +200 \text{ m s}^{-1}$ at the limb ($|y/R| = 1$).

Interestingly, the position-dependence of V_r^{hel} tends to be removed when the simulated convective blue-shift is subtracted, which finally makes the averaged shift for all the meridian data to be $\langle \langle V_r^{\text{hel,corr}} \rangle \rangle = 698 \text{ m s}^{-1}$ ($\sigma = 113 \text{ m s}^{-1}$).

Considering the ambiguities involved in the absolute wavelength calibration or in the correction due to convective Doppler shifts (at least several tens m s^{-1} , or more likely up to $\lesssim 100 \text{ m s}^{-1}$), we may state that this value is well consistent with the expected value of $+633 \text{ m s}^{-1}$ (due to the gravitational potential on the solar surface) as predicted from the general relativity theory. This means that we could confirm the solar gravitational redshift in a quantitatively satisfactory level within the precision of our analysis.

Acknowledgements Y. Takeda heartily thanks Dr. H. Knöckel for kindly providing the “IodineSpec” program, which turned out very helpful for checking the absolute wavelength scale of the reference I_2 spectrum.

Appendix

Analytical Formulation of Balthasar’s (1984) Empirical Limb-Effect

Balthasar (1984) carried out an empirical investigation on the center-to-limb variation of spectral-line shift on the solar disk and found that the trend of line-asymmetry as well as of line-shift depends on the formation heights of line cores ($\log \tau_B$). He tried to fit the observed shifts of many spectral lines by a quadratic polynomial in terms of $1 - \mu$ ($\mu \equiv \cos \theta$: direction cosine) as

$$\Delta \lambda_B \text{ (or } \Delta v_B) = a + b(1 - \mu) + c(1 - \mu)^2. \quad (19)$$

and determined the coefficients (a, b, c) for 6 different $\log \tau_B$ ranges (*cf.* Table IV therein), as shown in Figures 11a–11c. For practical convenience, we derived the

analytical expression of a , b , and c with respect to $\log \tau_B$ by applying quadratic least-square fitting to these data as

$$\begin{aligned} a \text{ (m}\mathring{\text{A}}) &= 0.254 + 0.619(\log \tau_B) + 0.138(\log \tau_B)^2, \\ b \text{ (m}\mathring{\text{A}}) &= -7.03 + 0.00450(\log \tau_B) + 0.819(\log \tau_B)^2, \\ c \text{ (m}\mathring{\text{A}}) &= 18.4 + 1.90(\log \tau_B) - 0.530(\log \tau_B)^2, \end{aligned} \quad (20)$$

as depicted in these figures. Considering that Balthasar (1984) used 5000 $\mathring{\text{A}}$ as the standard wavelength, we can convert these coefficients into velocity scale as

$$\begin{aligned} a \text{ (m s}^{-1}\text{)} &= 15.3 + 37.1(\log \tau_B) + 8.30(\log \tau_B)^2, \\ b \text{ (m s}^{-1}\text{)} &= -421.8 + 2.70(\log \tau_B) + 49.1(\log \tau_B)^2, \\ c \text{ (m s}^{-1}\text{)} &= 1100. + 113.9(\log \tau_B) - 31.8(\log \tau_B)^2. \end{aligned} \quad (21)$$

One problem is that Balthasar (1984) did not clarify the definition of his “line-core formation depth” (expressed as “lg τ ” therein but denoted here as $\log \tau_B$). We computed $\langle \log \tau \rangle$ and $\log \tau_0$ (the mean formation depth and the line-center formation depth defined in Equations (4) and (5)) for all 143 lines given in Table I of Balthasar (1984) in the same way as we did in Section 3.3. These results are compared with his $\log \tau_B$ values in Figures 11d and 11e, where we can see that his $\log \tau_B$ is similar to our $\log \tau_0$, though both are not in a linear relationship with each other. We found from least-squares analyses the following relations:

$$\langle \log \tau \rangle = -0.0375 + 1.03(\log \tau_B) + 0.124(\log \tau_B)^2, \quad (22)$$

$$\log \tau_0 = 0.0136 + 1.54(\log \tau_B) + 0.111(\log \tau_B)^2. \quad (23)$$

In the practical application in Section 5, our $\log \tau_0$ is converted into $\log \tau_B$ by using Equation (23) for each line, from which the necessary coefficients (such as b or c) can be derived by applying Equation (21).

References

- Allende Prieto, C., García López, R.J.: 1998, *Astron. Astrophys. Suppl.* **131**, 431.
 Balthasar, H.: 1984, *Solar Phys.* **93**, 219.
 Balthasar, H.: 1985, *Solar Phys.* **99**, 31.
 Beckers, J.M.: 1977, *Astrophys. J.* **213**, 900.
 Beckers, J.M., Nelson, G.D.: 1978, *Solar Phys.* **58**, 243.
 Blamont, J.E., Roddier, F.: 1961, *Phys. Rev. Lett.* **7**, 437.
 Borrero, J.M., Bellot Rubio, L.R.: 2002, *Astron. Astrophys.* **385**, 1056.
 Cacciani, A., Briguglio, R., Massa, F., Rapex, P.: 2006, *Celes. Mech. Dyn. Astron.* **95**, 425.
 Cox, A.N.: 2000, *Allen’s Astrophysical Quantities*, 4th ed. Springer, Berlin, 69.
 Dravins, D.: 1982, *Annu. Rev. Astron. Astrophys.* **20**, 61.
 Einstein, A.: 1911, *Ann. Phys. (Germany)* **35**, 898.
 Forbes, E.G.: 1961, *Annals of Science* **17**, 129.
 Halm, J.: 1907, *Astron. Nachr.* **173**, 273.
 Knöckel, H., Bodermann, B., Tiemann, E.: 2004, *Eur. Phys. J. D* **28**, 199.
 Kurucz, R.L.: 1993, *Kurucz CR-ROM No. 13*, Harvard-Smithsonian Center for Astrophysics, Cambridge, MA.

-
- Kurucz, R.L., Bell, B.: 1995, *Kurucz CR-ROM No. 23*, Harvard-Smithsonian Center for Astrophysics, Cambridge, MA.
- Leushin, V.V., Topil'skaya, G.P.: 1987, *Astrophysics* **25**, 415.
- LoPresto, J.C., Chapman, R.D., Sturgis, E.A.: 1980, *Solar Phys.* **66**, 245.
- LoPresto, J.C., Schrader, C., Pierce, A.K.: 1991, *Astrophys. J.* **376**, 757.
- Marcy, G.W., Butler, R.P.: 1992, *Publ. Astron. Soc. Pacific* **104**, 270.
- Nakai, Y., Hattori, A.: 1985, *Mem. Fac. Sci., Kyoto Univ., Ser. A, Phys., Astrophys., Geophys. Chem.* **36**, 385.
- Neckel, H.: 1994, In: Pap, J.M., Frolich, C., Hudson, H.S., Solanki, S. (eds.), *The Sun as a Variable Star, Solar and Stellar Irradiance Variations, IAU Coll.* **143**, 37.
- Neckel, H.: 1999, *Solar Phys.* **184**, 421.
- Pierce, A.K., Breckinridge, J.B.: 1972, *The Kitt Peak Table of Photographic Solar Spectrum Wavelength, Kitt Peak Contribution No. 559*.
- Pound, R.V., Rebka, G.A.: 1960, *Phys. Rev. Lett.* **4**, 337.
- Schröter, E.H.: 1959, *Mitt. Astrophys. Obs. Potsdam* **83**, 69.
- Snider, J.L.: 1970, *Solar Phys.* **12**, 352.
- Snider, J.L.: 1972, *Phys. Rev. Lett.* **28**, 853.
- Takeda, Y.: 1995, *Publ. Astron. Soc. Japan* **47**, 287.
- Takeda, Y., Sato, B., Kambe, E., Watanabe, E., Miyazaki, H., Wada, S., et al.: 2002, *Publ. Astron. Soc. Japan* **54**, 113.
- Takeda, Y., Ueno, S.: 2011, *Solar Phys.* **270**, 447 (Paper I).
- Vessot, R.F.C., Levine, M.W., Mattison, E.M., Blomberg, E.L., Hoffman, T.E., Nystrom, G.U., Farrel, B.F., Decher, R., Eby, P.B., Baugher, C.R.: 1980, *Phys. Rev. Lett* **45**, 2081.

Table 1. Solar gravitational redshift determinations over the last 50 years (expressed by $R \equiv \Delta_{\text{obs}}/\Delta_{\text{the}}$).

<p>Authors: Blamont and Roddier (1961) Method: Sr I 4607 line with atomic-beam resonant scattering method Results: $R \approx 0.5$ ($\approx 5 \text{ m}\text{\AA}/9.76 \text{ m}\text{\AA}$) [disk center], $R \approx 1.0$ ($\approx 10 \text{ m}\text{\AA}/9.76 \text{ m}\text{\AA}$) [limb] Remark: Redshift of $2.4 \text{ m}\text{\AA}$ due to Stark effect is subtracted</p>
<p>Authors: Snider (1970) Method: K I 7699 line with atomic-beam resonant scattering method Results: $R = 0.61 \pm 0.06$ ($10 \pm 1 \text{ m}\text{\AA}/16.3 \text{ m}\text{\AA}$) [disk center]</p>
<p>Authors: Snider (1972) Method: K I 7699 line with atomic-beam resonant scattering method Results: $R = 1.01 \pm 0.06$ ($16.4 \pm 1 \text{ m}\text{\AA}/16.3 \text{ m}\text{\AA}$) [disk center]</p>
<p>Authors: Beckers (1977) Method: Measuring line-shifts of Zeeman-insensitive ($g = 0$) Ti I 5713 line in the umbrae of 7 sunspots Results: $R = 0.97 \pm 0.02$ ($613 \pm 14 \text{ m s}^{-1}/633 \text{ m s}^{-1}$)</p>
<p>Authors: LoPresto <i>et al.</i> (1980) Method: 738 Fe lines based on Pierce and Breckinridge's (1972) wavelength table (disk center) Results: $R = 0.76 \pm 0.24$ (all 738 lines at 2930–5762 Å), $R = 0.97 \pm 0.16$ (only 74 strong lines at 3075–4958 Å)</p>
<p>Authors: LoPresto <i>et al.</i> (1991) Method: Wavelength shifts (at the profile core) of oxygen triplet lines at 7772–7775 Å Results: $R = 0.73$ ($460 \text{ m s}^{-1}/633 \text{ m s}^{-1}$) [disk center], $R = 0.99$ ($627 \text{ m s}^{-1}/633 \text{ m s}^{-1}$) [limb] Remark: Measurements on 7 different points suggest a tendency of increasing shifts toward the limb</p>
<p>Authors: Cacciani <i>et al.</i> (2006) Method: Doppler shift measurements over a number of points over the disk by using a magneto-optical filter Results: $R = 0.99$ ($625 \text{ m s}^{-1}/633 \text{ m s}^{-1}$) [at the meridian line of zero-rotational velocity] Remark: Several assumptions are involved regarding other sources causing line shifts (<i>cf.</i> section 6.1 therein)</p>

Note: The theoretical solar gravitational redshift of 633 m s^{-1} (the value corresponding to observations from the earth) is adopted here.

Table 2. Atomic and relevant data of important lines at each region of spectrum fitting.

Species	λ_{air} (Å)	χ_{low} (eV)	$\log gf$	Gammar	Gammas	Gammaw	EW (mÅ)	$\langle \log \tau \rangle$	$\log \tau_0$	δV_1 (m s ⁻¹)
Region (a): 5188.5–5193.6 Å (Fe, Ti, Ca, Cr, Ni, and Nd abundances varied to adjust)										
Ti II	5188.680	1.582	-1.210	8.23	-6.66	-7.95	91.7	-1.52	-2.42	-249.6
Ca I	5188.844	2.932	-0.090	8.42	-4.18	-7.31	124.2	-1.10	-2.08	-262.9
Ti I	5189.621	2.239	-1.017	8.06	-5.71	-7.79	3.7	-0.06	-0.07	
Fe I	5191.455	3.038	-0.656	8.00	-5.47	-7.62	176.4	-1.69	-3.68	-294.5
Cr I	5192.002	3.395	-0.390	7.91	-5.32	-7.62	23.2	-0.33	-0.48	
Fe I	5192.343	2.998	-0.521	8.01	-5.47	-7.62	204.3	-1.64	-3.92	-282.3
Ni I	5192.490	3.699	-1.512	8.08	-5.67	-7.69	26.7	-0.41	-0.60	
Nd II	5192.614	1.136	0.290	7.92	-5.80	-7.73	8.7	-0.15	-0.22	
Ti I	5192.969	0.021	-1.006	6.78	-6.32	-7.84	84.6	-1.78	-2.63	-247.1
Cr I	5193.480	3.422	-0.720	6.83	-6.11	-7.84	11.9	-0.16	-0.23	
Region (b): 5193.6–5199.0 Å (Fe, Cr, Mn, Ni, Ti, and Y abundances varied to adjust)										
Ti I	5194.034	2.103	-0.560	7.83	-5.37	-7.62	10.2	-0.13	-0.19	
Fe I	5194.941	1.557	-2.090	6.29	-6.20	-7.87	120.7	-2.26	-3.74	-298.9
Fe I	5195.468	4.220	-0.002	8.31	-6.17	-7.67	102.9	-1.43	-2.40	-277.0
Fe I	5196.077	4.256	-0.451	8.33	-5.16	-7.67	77.4	-1.16	-1.80	-240.6
Y II	5196.422	1.748	-0.880	7.92	-5.93	-7.77	22.5	-0.37	-0.53	
Cr I	5196.482	3.449	-0.270	7.80	-5.93	-7.82	21.1	-0.30	-0.44	
Cr I	5196.590	3.449	-0.360	7.83	-5.94	-7.82	18.0	-0.25	-0.37	
Mn I	5196.593	3.135	-0.930	7.77	-6.09	-7.83	9.5	-0.13	-0.19	
Ni I	5197.157	3.898	-1.190	8.14	-5.59	-7.81	21.7	-0.32	-0.47	
Fe II	5197.577	3.230	-2.100	8.48	-6.60	-7.95	86.8	-1.17	-1.93	-250.3
Fe I	5197.929	4.301	-1.340	8.33	-4.77	-7.77	31.7	-0.47	-0.69	
Fe I	5198.711	2.223	-2.135	8.21	-6.18	-7.83	87.5	-1.67	-2.55	-253.3
Region (c): 5199.0–5205.0 Å (Cr, Fe, Y, Nd, and Ti abundances varied to adjust)										
Fe I	5199.531	3.882	-3.236	8.01	-5.47	-7.69	1.5	-0.03	-0.04	
Fe I	5199.695	3.546	-3.248	7.69	-6.11	-7.80	2.9	-0.05	-0.06	
Nd II	5200.121	0.559	-0.490	7.92	-5.89	-7.75	10.4	-0.18	-0.27	
Cr I	5200.207	3.385	-0.660	7.91	-5.34	-7.62	14.7	-0.20	-0.29	
Y II	5200.406	0.992	-0.570	7.92	-6.03	-7.80	31.5	-0.56	-0.83	
Ti I	5201.119	2.092	-0.749	7.83	-5.37	-7.62	6.3	-0.08	-0.12	
Fe I	5202.251	4.256	-0.639	8.32	-5.88	-7.67	66.7	-1.02	-1.55	-229.9
Fe I	5202.335	2.176	-1.838	8.23	-6.18	-7.83	103.8	-1.89	-3.02	-279.5
Cr I	5204.506	0.941	-0.208	7.72	-6.15	-7.86	164.5	-2.22	-4.28	-307.6
Fe I	5204.582	0.087	-4.332	3.76	-6.33	-7.89	82.3	-1.98	-2.91	-231.0
Region (d): 5205.0–5211.0 Å (Cr, Fe, Ti, and Y abundances varied to adjust)										
Fe I	5205.309	4.260	-2.673	7.99	-5.16	-7.67	4.0	-0.06	-0.08	
Y II	5205.724	1.033	-0.340	7.91	-6.03	-7.80	43.7	-0.82	-1.23	
Cr I	5206.038	0.941	0.019	7.72	-6.15	-7.86	208.6	-2.08	-4.65	-292.5
Ti I	5206.119	2.487	1.070	7.80	-6.12	-7.84	51.7	-0.85	-1.24	
Cr I	5206.203	2.708	-1.283	8.36	-5.46	-7.57	17.4	-0.24	-0.36	
Cr I	5206.561	3.435	-1.251	6.98	-5.89	-7.82	4.5	-0.07	-0.09	
Fe I	5206.594	4.294	-2.908	7.90	-4.52	-7.59	2.2	-0.04	-0.05	
Fe I	5206.801	4.283	-2.530	8.31	-4.32	-7.76	5.3	-0.07	-0.10	
Fe I	5207.939	3.635	-2.450	8.30	-6.05	-7.84	20.7	-0.31	-0.46	
Cr I	5208.112	2.709	-1.772	8.36	-5.46	-7.57	6.4	-0.09	-0.12	
Cr I	5208.419	0.941	0.158	7.72	-6.15	-7.86	234.0	-1.99	-4.81	-279.7
Fe I	5208.593	3.241	-0.980	7.88	-5.51	-7.62	114.7	-1.64	-2.84	-291.2
Fe I	5209.884	3.237	-3.460	7.31	-6.29	-7.87	5.9	-0.09	-0.12	
Ti I	5210.386	0.048	-0.884	6.77	-6.31	-7.84	73.1	-1.52	-2.21	-227.8
Cr II	5210.865	3.758	-2.945	8.42	-6.46	-7.89	5.0	-0.07	-0.10	

Shown here are the atomic data of the lines of appreciable strengths (see also Figure 2), which were taken from Kurucz & Bell’s (1995) compilation (with adjustments for 4 lines; *cf.* Section 3.2). Followed by first four self-explanatory columns, damping parameters are presented in columns 5–7: Gammar is the radiation damping width (s⁻¹), $\log \gamma_{\text{rad}}$. Gammas is the Stark damping width (s⁻¹) per electron density (cm⁻³) at 10⁴ K, $\log(\gamma_e/N_e)$. Gammaw is the van der Waals damping width (s⁻¹) per hydrogen density (cm⁻³) at 10⁴ K, $\log(\gamma_w/N_H)$. In case where these damping parameters are not given in Kurucz and Bell (1995), they were computed as default values in Kurucz’s WIDTH program (Leushin and Topil’skaya, 1987). Columns 8–10 give the strength-related quantities relevant to the disk-center spectrum (*cf.* Section 3.3): the equivalent width inversely computed from the best-fit abundance solution (*cf.* Figure 2) under the assumption of isolated single line, the mean depth of line formation, and the line-center formation depth. Presented in column 11 is the theoretically estimated convective blue-shift at $\mu = 1$ (only for the representative 18 lines; *cf.* Section 5.2).

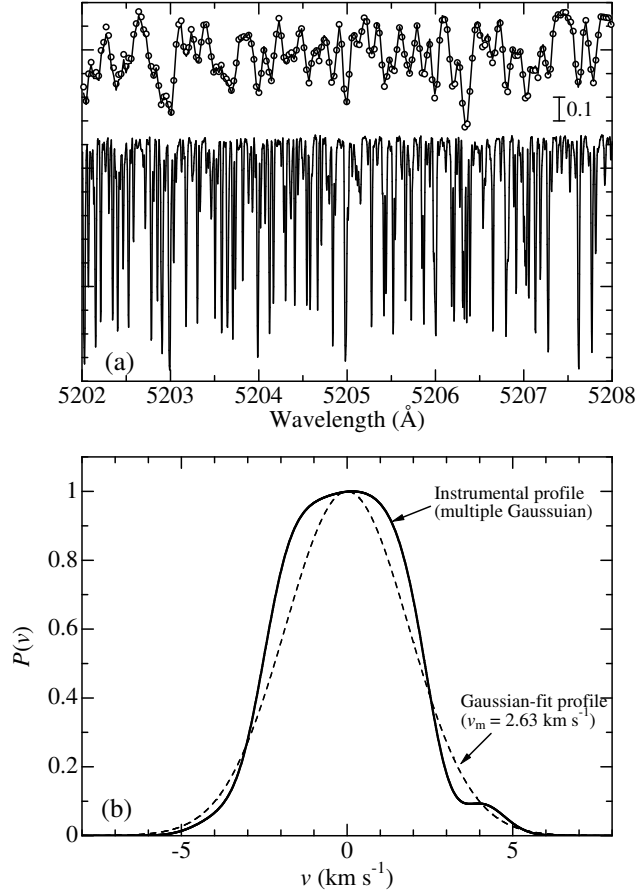


Figure 1. Determination of the instrumental profile (P_λ) by comparing the observed lamp+I₂ spectrum (D_λ^{obs}) with the simulated spectrum ($D_\lambda^{\text{sim}} \equiv T_\lambda \otimes P_\lambda$, where T_λ is the transmission function of I₂ vapor). (a) Upper spectra are the observed D_λ^{obs} (open circles) with the best-fit D_λ^{sim} (solid line) overplotted, while the lower spectrum (solid line) is T_λ . (b) Thick solid line is the finally obtained $P(v)$ (the sum of nine off-center Gaussian functions; *cf.* Section 2), while the dashed line is the special case derived by assuming that P is the Gaussian form. The abscissa is in the velocity scale, and both profiles are normalized at the maximum peak to be unity.

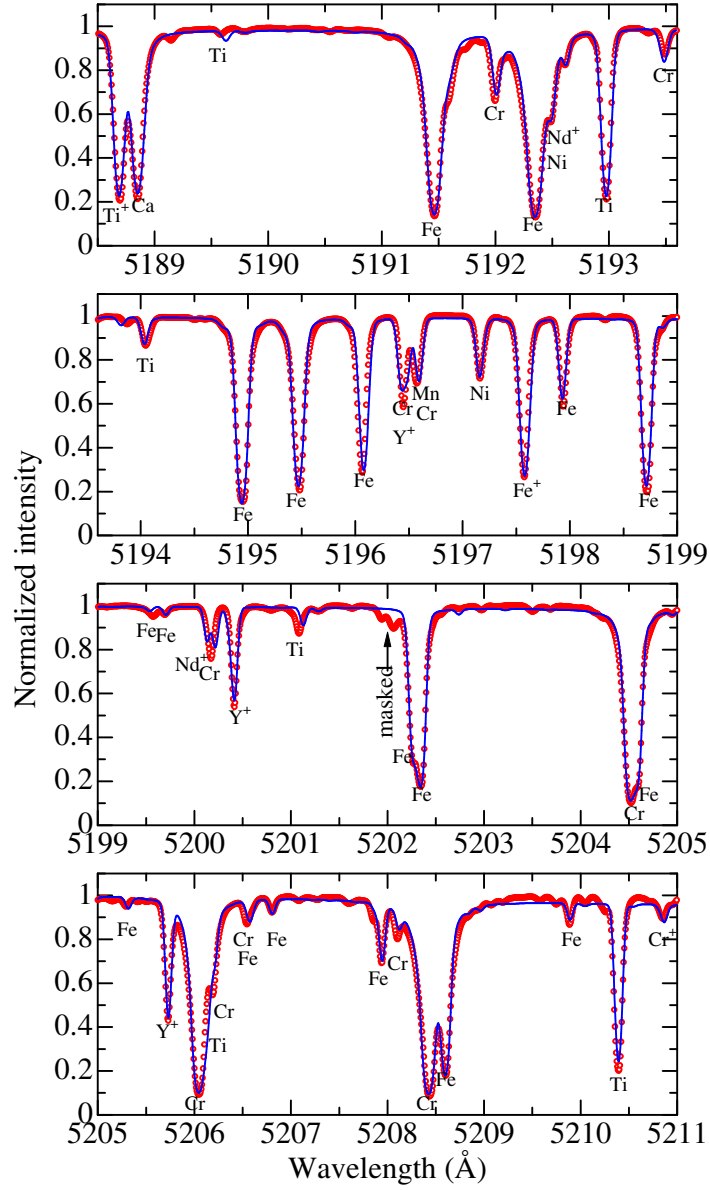


Figure 2. Demonstration of how the solar intensity spectrum simulated at $\mu = 1$ for each wavelength region (a–d) can be fitted with the observed solar disk-center spectrum (Neckel, 1994, 1999) by adjusting the abundances and the macrobroadening parameter. Observed and theoretical spectrum are expressed by (red) open circles and (blue) solid lines, respectively. Identifications are given for the line features of appreciable strengths.

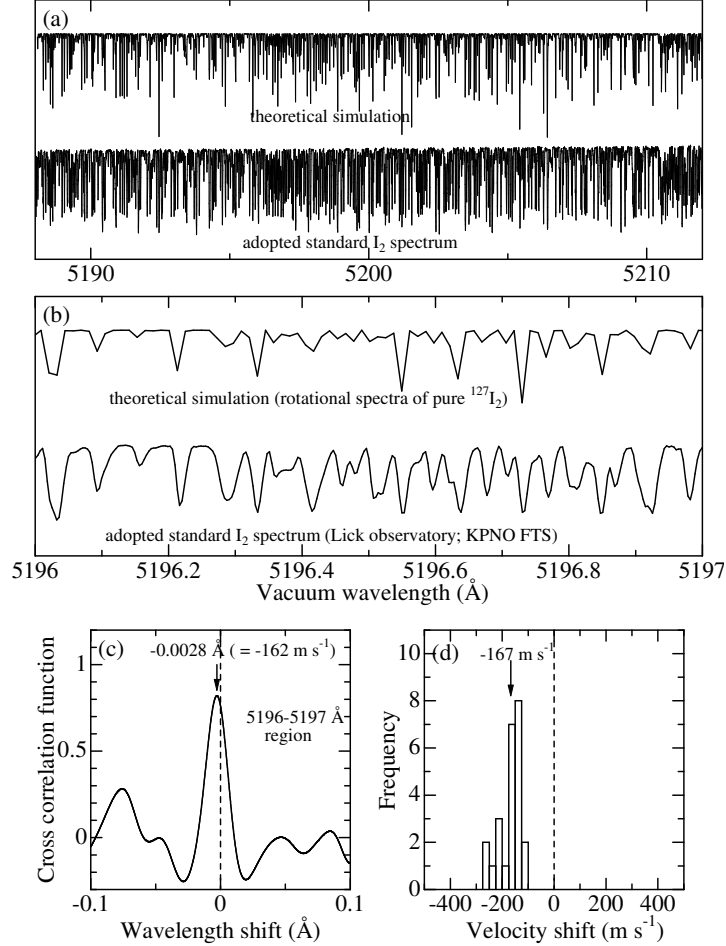


Figure 3. Comparison of the theoretical pure ¹²⁷I₂ absorption spectrum simulated by Knöckel *et al.*'s (2004) “IodineSpec” program with the observed I₂ absorption spectrum (Lick I₂ cell spectrum recorded with Kitt Peak FTS) adopted as the reference in this study: (a) wide view for the 5188–5212 Å region and (b) magnified view for the 5196–5197 Å region (note that vacuum wavelength scale is used in these two figures). (c) Result of cross-correlation analysis for the 5196–5197 Å region shown in panel (b), where the abscissa corresponds to the wavelength correction to be applied to the observed spectrum to enable a match between the two. (d) Histogram showing the distribution of the corrections (expressed in the velocity scale) derived by cross-correlation analyses for each of the twenty-four 1 Å bins in the 5188–5212 Å region.

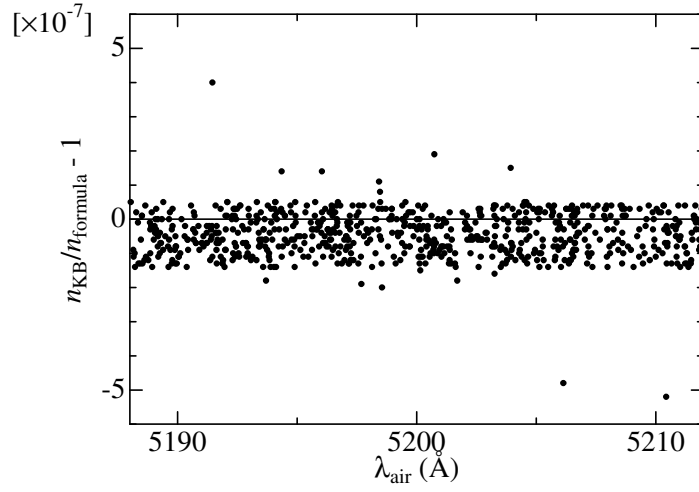


Figure 4. Wavelength-dependence of the relative difference between n_{formula} and n_{KB} (two kinds of refractive indices) for all the spectral lines at $5188\text{\AA} \leq \lambda_{\text{air}} \leq 5212\text{\AA}$ included in Kurucz and Bell's (1995) compilation, where n_{formula} is the refractive index of air based on the standard formula given in Cox (2000) as given in Equation (7) while n_{KB} is estimated from Kurucz and Bell's (1995) atomic data by Equation (8).

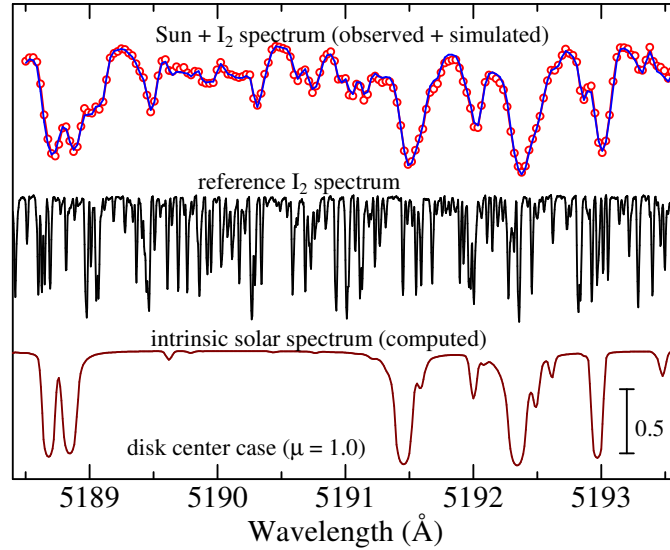


Figure 5. Graphical example [for the disk-center case at region (a)] of how the absolute wavelength shift can be determined by searching for the best-fit parameters such those accomplishing the best-fit (simulated) $I_{\lambda,\text{th}} [\equiv G_{\lambda} \otimes (T_{\lambda} \cdot I_{\lambda,\text{intr}})]$; cf. Equation (2)] with the observed $I_{\lambda,\text{obs}}$ (observed solar intensity spectrum recorded through the I_2 absorption cell. Top: comparison of $I_{\lambda,\text{obs}}$ (red open circles) and $I_{\lambda,\text{th}}$ (blue solid line). Middle: T_{λ} (transmission spectrum of I_2 vapor cell). Bottom: $I_{\lambda,\text{intr}}$ (computed intrinsic solar intensity spectrum).

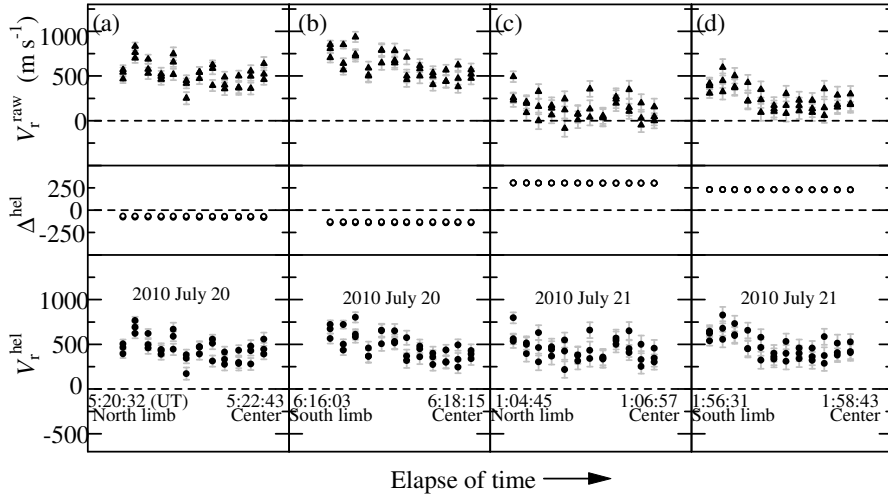


Figure 6. Runs of derived raw radial velocities (V_r^{raw}), heliocentric corrections (Δ^{hel}), and heliocentric radial velocities (V_r^{hel}) with time, for four kinds of scanning observations along the solar meridian line relevant for this study, each of which were carried out from the limb to the disk center over ≈ 2 minutes. The results for the 2010 July 20 observations (east–west aligned slit) are shown in panels (a) ($\theta = 0^\circ$; northern meridian) and (b) ($\theta = 180^\circ$; southern meridian). Similarly, those for the 2010 July 21 observations (north–south aligned slit) are presented in panels (c) and (d). In each panel, the horizontal dashed line denotes the zero-level.

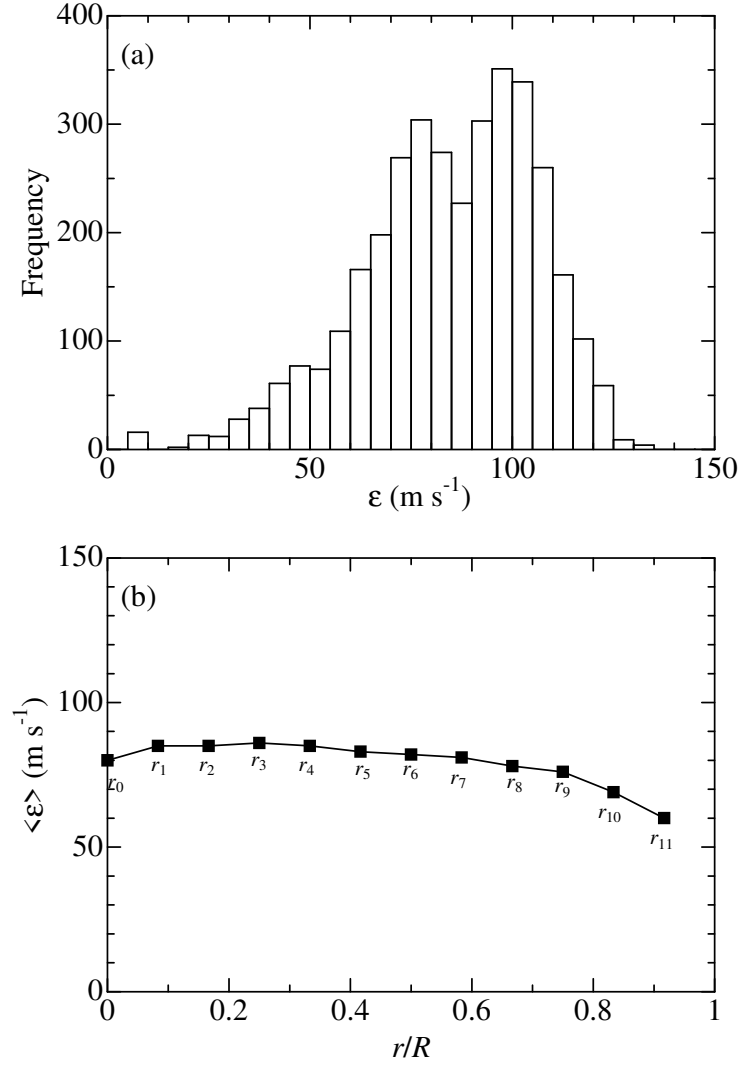


Figure 7. (a) Distribution histogram for the probable error (ϵ) in V_r (where results all over the disk are combined). (b) Mean probable errors ($\langle \epsilon \rangle$; averaged at the same radius bin) plotted against the radius.

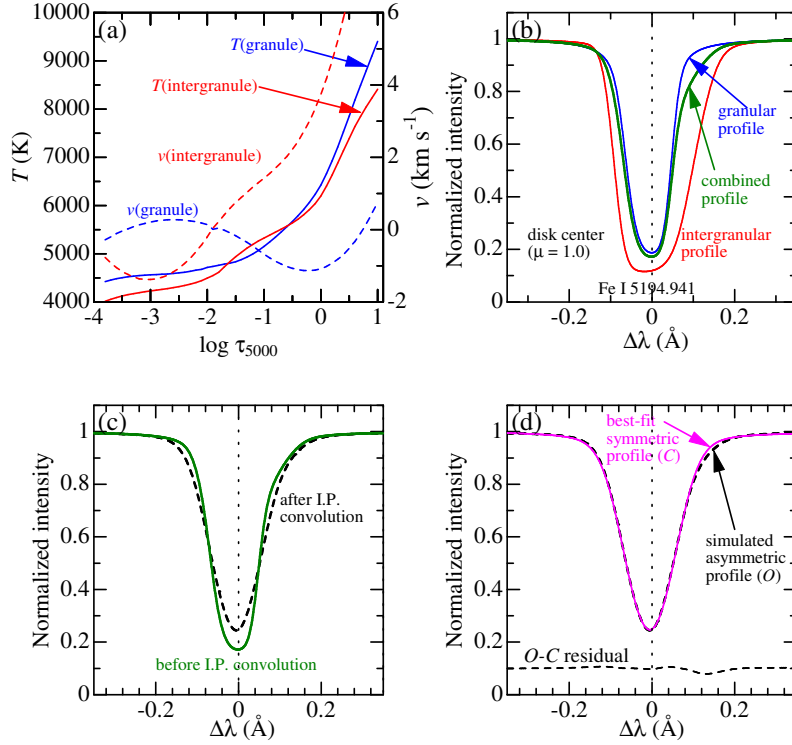


Figure 8. (a) $T(\tau_{5000})$ (solid line) and $v(\tau_{5000})$ (dashed line; positive for the downflow) structures of two-component solar photospheric model (blue and red lines corresponding to granular and intergranular region, respectively) derived by Borrero and Bellot Rubio (2002), which we adopted for the line-profile simulation. (b) Illustration of how the realistic asymmetric profile (green) is produced as a combination of granular (blue) and intergranular (red) profiles (being weighted according to the filling factor and the continuum intensity), for the case of Fe I 5194.941 line at the disk-center. (c) Example of how the simulated profile (green solid line) in (b) is broadened to result in a realistic profile (black dashed line) corresponding to our observation by convolving the instrumental profile (*cf.* thick solid line in Figure 1b). (d) Demonstration of how the asymmetric profile simulated in (c) (black-dashed line) can be fitted with the classically-modeled symmetric profile (pink solid line) by adjusting the profile parameters (Fe abundance, line broadening parameter v_M , and the line shift). The $O - C$ residual is also shown at the bottom of the figure (with an offset of +0.1).

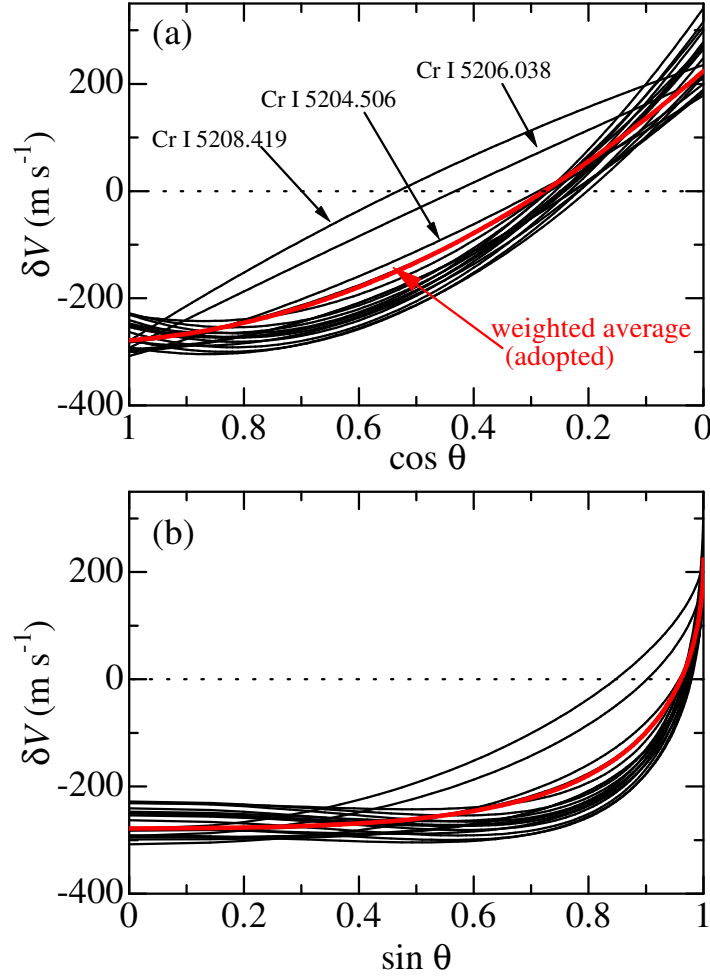


Figure 9. Angle/position-dependent convective line shifts (δV) for 18 representative lines of appreciable strengths, which were simulated based on Borrero and Bellot Rubio's (2002) two-component model for the disk center (δV_1) and combined with Balthasar's (1984) empirical $\delta V_\mu - \delta V_1$ relation (cf. Section 5.3 and Appendix). (a) δV vs. $\cos \theta$ ($\equiv \mu$), (b) δV vs. $\sin \theta$ ($\equiv y/R$). The finally adopted relation (averaged over 18 lines) is depicted by the thick red line.

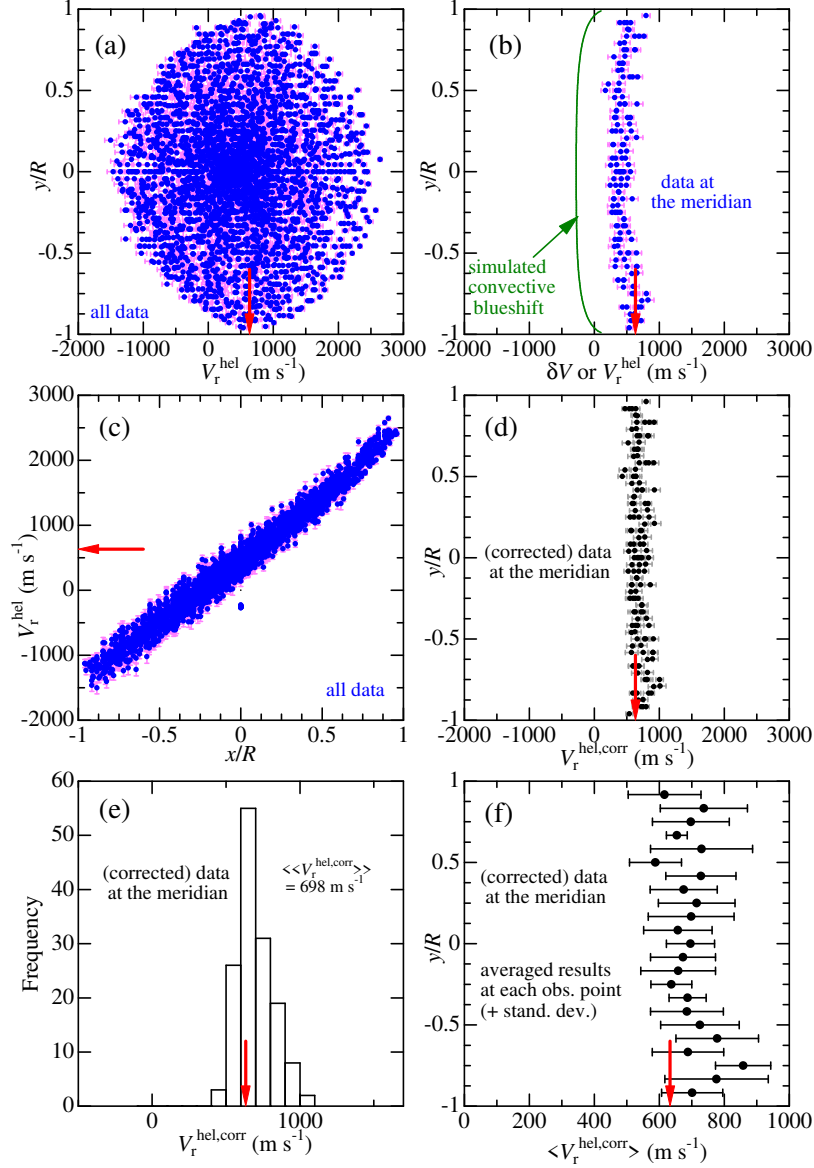


Figure 10. Behaviors of the V_r^{hel} (absolute heliocentric Doppler shift in m s^{-1}) at various positions of the solar disk (x coordinate: E–W direction increasing toward west, y coordinate: S–N direction increasing toward north); expressed in unit of the solar radius R). (a) V_r^{hel} vs. y for all measurements over the entire disk. (c) x vs. V_r^{hel} for all measurements over the entire disk. (b) V_r^{hel} vs. y only for the meridian measurements ($x = 0$). The positional-dependence of the simulated convective shift [$\langle \delta V_\mu \rangle$; cf. Equation (17)], which is a function of y through the relation $\mu = \sqrt{1 - (x^2 + y^2)/R^2} = \sqrt{1 - (y/R)^2}$ is also depicted by the solid line. (d) $V_r^{\text{hel,corr}}$ ($\equiv V_r^{\text{hel}} - \langle \delta V_\mu \rangle$) vs. y only for the meridian measurements ($x = 0$). (e) Histogram showing the distribution of $V_r^{\text{hel,corr}}$. (f) $\langle V_r^{\text{hel}} \rangle$ vs. y , where $\langle V_r^{\text{hel}} \rangle$ is the average of data at almost the same meridian points (bars indicate the standard deviation). In panels (a)–(d), probable errors involved for each of the V_r measurements are indicated by thin ticks. The expected solar gravitational redshift at the earth (633 m s^{-1}) is shown by the (red) arrow in all six panels.

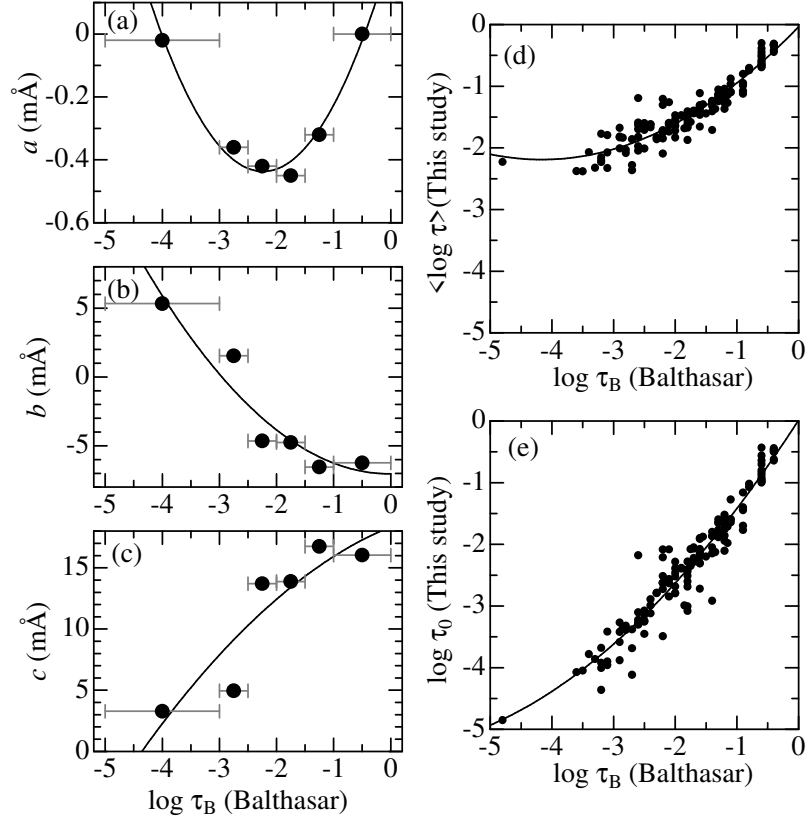


Figure 11. Panels (a)–(c): Graphical representation of the depth-dependence of the coefficients (a , b , c) used for the polynomial fits of the limb effect, $\Delta\lambda = a + b(1 - \mu) + c(1 - \mu)^2$, which were empirically determined by Balthasar (1984; *cf.* Table IV therein). The quadratic dependence of these coefficients in terms of $\log \tau_B$, which we derived from the least-squares fit are also depicted. Panels (d) and (e) show the relationships between the line-core-forming depth ($\log \tau_B$) adopted by Balthasar (1984) and the two kinds of line-formation depths ($\langle \log \tau \rangle$ and $\log \tau_0$; *i.e.*, mean depth of line formation and the line-center-forming depth) derived in this study. The least-squares fitted quadratic relations are also drawn.